

# Wall-modeled large-eddy simulation of the Sandia Axisymmetric Transonic Bump

By A. Elnahas, R. Agrawal AND P. Moin

## 1. Motivation and objectives

The prediction of complex flow phenomena such as three-dimensional juncture flows (Lee & Pulliam 2019), smooth-body separation (Rumsey *et al.* 2019), and transonic shock-induced boundary layer separation (Vassberg *et al.* 2008) are necessary steps towards the accurate prediction of engineering quantities of interest (QoIs) on modern aircraft using computational fluid dynamics (CFD). Wall-modeled large-eddy simulation (WMLES) has shown great potential for accurately predicting such flow phenomena. In large-eddy simulation (LES), the large, energy-carrying eddies are resolved on the grid, and the effect of the small, dissipative scales on these large eddies is encapsulated in a subgrid-scale (SGS) model (Rogallo & Moin 1984; Meneveau & Katz 2000). In the presence of walls, the energy-carrying eddies scale linearly with distance from the wall, causing wall-resolved LES calculations to remain prohibitively expensive (Choi & Moin 2012; Yang & Griffin 2021). WMLES is a paradigm where the prohibitively expensive near-wall region of a wall-bounded turbulent flow is replaced with a reduced-order model, whose role is to provide the stress at the wall (Bose & Park 2018). WMLES has been successfully applied to predict three-dimensional juncture flows using the NASA juncture flow experiment (Lozano-Durán *et al.* 2020, 2022), and smooth-body separation using the Boeing smooth-body separation experiment (Agrawal *et al.* 2022). This brief aims to assess the predictive capability of WMLES in another complex case, namely transonic shock-induced boundary layer separation, by simulating the Sandia Axisymmetric Transonic Bump (ATB) (Lynch *et al.* 2019, 2020; Beresh *et al.* 2020; Lynch 2022).

The Sandia ATB is a recent experiment that revisits the canonical flow experiments by Bachalo & Johnson (1986), where the effects of transonic shock-induced and smooth-body separation coexist. In the Sandia ATB experiment, a trip causes a fully turbulent boundary layer to grow over the geometry, which is then accelerated through the favorable-pressure gradient region generated by the bump. When the flow over the bump becomes locally supersonic, the resulting shock separates the boundary layer on the aft side of the bump. Figure 1 showcases the experimental geometry and the shock-induced separation bubble. The experiment had two key objectives. The first was to provide more detailed measurements missing from the original Bachalo & Johnson (1986) experiment, such as skin friction measurements, planar particle-image velocimetry measurements of the mean velocity and second-order turbulent statistics, and unsteady shock location measurements, as well as an improved characterization of the geometry. The second was to reduce the Reynolds number relative to the original Bachalo & Johnson (1986) experiment so that the flow is computationally more tractable to high-fidelity scale-resolving simulations. These approaches can draw insights about the flow not available to traditional computational paradigms such as Reynolds-averaged Navier Stokes (RANS). It is important to note that the flow over the Sandia ATB is representative of the flow over an aircraft, such as the NASA Common Research Model (CRM) at

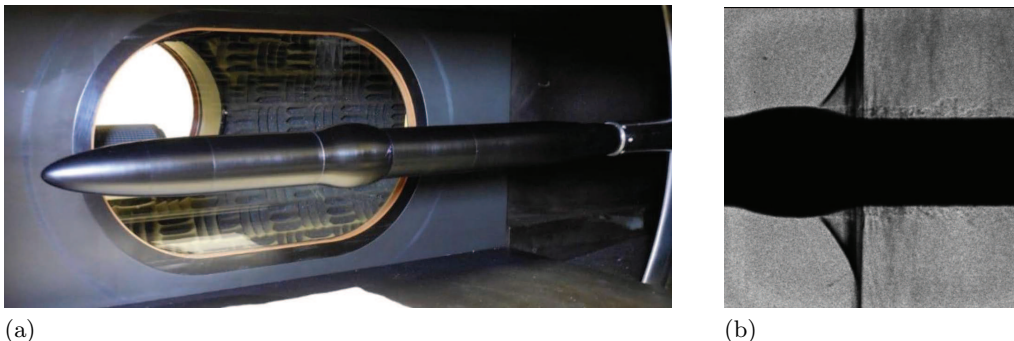


FIGURE 1. (a) The Sandia ATB mounted in the transonic test section of the Sandia Trisonic Wind Tunnel (Lynch *et al.* 2019). (b) A Schlieren visualization of the shock formed over the Sandia ATB (Lynch *et al.* 2019).

transonic cruise conditions. The experimental chord-based Reynolds number over the Sandia ATB,  $Re_c = 1 \times 10^6$ , corresponds to a friction Reynolds number of the attached boundary layer of  $Re_\tau \approx 800$ , which is within the range of measurements obtained from WMLES calculations of the transonic CRM (Goc 2023). Furthermore, the Mach number,  $Ma = 0.875$ , also matches the conditions over the transonic CRM (Vassberg *et al.* 2008). The Sandia ATB was the focus of a “blind” CFD challenge conducted between January 2020 and January 2021. Figure 2 shows the previous attempts at simulating this flow using both RANS and scale-resolving paradigms (Riley & Adler 2021; Gupta *et al.* 2021; Rahmani & Wang 2022). A key conclusion from this CFD challenge was that the scatter is large and that no single method can predict the correct skin-friction coefficient across all regions of the flow.

The remainder of this brief is structured as follows. Section 2 presents the computational framework, including the two different SGS models and the wall model employed. Section 3 describes the geometry, meshing strategy/grid resolution, and boundary conditions. Sections 4 and 5 quantify the sensitivity to the SGS model in predicting the two key engineering QoIs, namely the skin-friction and pressure coefficient distributions along the streamwise extent of the model, respectively. The results in those sections are compared to a new set of experimental measurements by Lynch (2022). Finally, conclusions and future tasks are presented in Section 6.

## 2. Computational framework

The flow around the Sandia ATB is simulated using a WMLES implementation in the GPU-accelerated charLES solver. CharLES is a cell-centered, unstructured, finite-volume solver that uses low-dissipation, entropy-preserving second-order spatial discretizations and a third-order Runge-Kutta scheme for time advancement (Goc *et al.* 2021). The governing equations are the implicitly filtered compressible Navier-Stokes equations with the SGS stress tensor defined as

$$\tau_{ij}^{SGS} = \tilde{\rho}(\overline{u_i u_j} - \overline{u_i} \overline{u_j}), \quad (2.1)$$

where  $(\tilde{\cdot})$  and  $(\overline{\cdot})$  denote the filtering and Favre-averaged filtering operations, respectively.  $\tilde{\rho}$  and  $\overline{u_i}$  are the filtered density and Favre-filtered velocity in the  $i$ th cardinal direction, respectively. For this brief, the deviatoric part of the SGS tensor is modeled

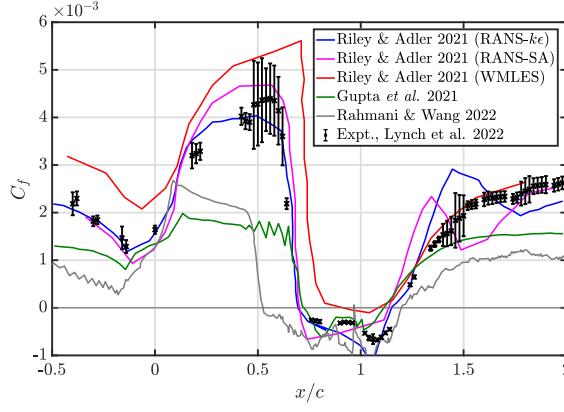


FIGURE 2. The skin-friction coefficient,  $C_f$ , azimuthally averaged over the surface of the Sandia ATB as a function of the streamwise distance normalized by the chord length predicted by various groups using both RANS and scale resolving paradigms. Refer to Riley & Adler (2021), Gupta *et al.* (2021), and Rahmani & Wang (2022) for the details of their implementations.

using either a single-coefficient or tensorial-coefficient eddy-viscosity model with the coefficients computed on the fly using a variation of the dynamic procedure of Germano *et al.* (1991) and Lilly (1992) based on local time averaging to regularize the least-squares problem. The isotropic component of  $\tau_{ij}^{SGS}$  is absorbed into a modified pressure.

The single-coefficient eddy-viscosity model is the dynamic Smagorinsky model (DSM), defined as

$$\tau_{ij}^{SGS} - \frac{\tau_{kk}^{SGS}}{3}\delta_{ij} = \tau_{ij}^{DSM} = -C\Delta^2\bar{\rho}\bar{S}_{ij}|\bar{S}|, \quad (2.2)$$

where  $\Delta$  is a measure of the grid-cell size, and  $C$  is an unknown constant *a priori*. The combined coefficient  $C\Delta^2$  is solved for using the locally/temporally averaged least-squares Germano identity. The tensorial-coefficient eddy-viscosity model is the dynamic tensorial-coefficient Smagorinsky model (DTCSM) of Agrawal *et al.* (2022), where the Boussinesq assumption is relaxed and is defined as

$$\tau_{ij}^{SGS} - \frac{\tau_{kk}^{SGS}}{3}\delta_{ij} = \tau_{ij}^{DTCSM} = -(C_{ik}\bar{S}_{kj} + C_{jk}\bar{S}_{ki})\Delta^2\bar{\rho}|\bar{S}|, \quad (2.3)$$

with the tensorial coefficients related in the following manner

$$C_{11} = C_{22} = C_{33}; \quad C_{ij} = -C_{ji} \text{ for } (i \neq j). \quad (2.4)$$

The reasoning for these relationships and more details are presented by Agrawal *et al.* (2022). The remaining four coefficients are also solved for using the locally/temporally averaged least-squares Germano identity.

An equilibrium stress wall model is used to predict the wall-shear stress, which is applied through a Neumann boundary condition (Bose & Park 2018; Kawai & Larsson 2013). This model captures the effect of the prohibitively expensive near-wall region of the wall-bounded turbulent flow. At each grid cell near the wall, the velocity at the cell's centroid is used as an input to the algebraic wall model to predict the stress. Goc *et al.* (2021) showed that this first-cell matching procedure is successful on complex geometries, particularly with the hexagonal-close packed (HCP) mesh structure employed in these calculations.

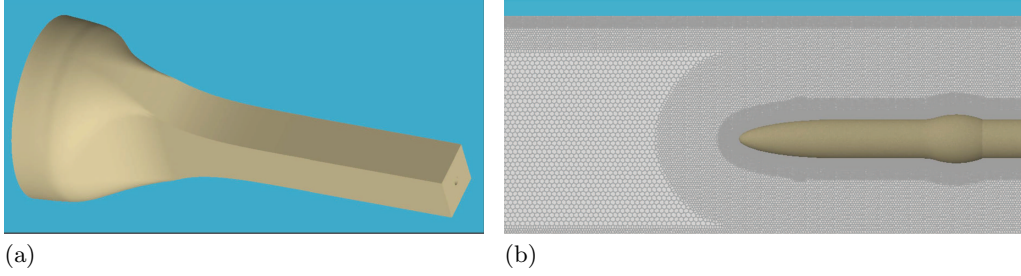


FIGURE 3. (a) The simulated wind tunnel geometry. (b) A representation of the HCP mesh used to simulate the flow over the Sandia ATB. This visualization represents the coarsest mesh resolution.

### 3. Geometry, meshing, and boundary conditions

The calculations carried out in this brief reproduced the experimental configuration as closely as possible, given the available characterization of the facility. Figure 1(a) shows the Sandia ATB placed in the Sandia Trisonic Wind Tunnel facility, which is included in the simulation domain, as shown in Figure 3(a). The mesh used in the WMLES calculations is constructed based on truncated Voronoi diagrams constructed from an HCP seeding of points in space. The mesh is homothetically refined with distance from the wall. This refinement strategy follows the geometric scaling of the energy-containing eddies of Townsend (1976). Three mesh resolutions are tested, and the resolution is quantified using the number of grid points within the boundary layer upstream of the favorable-pressure gradient region of the bump. These values and the total number of grid points for each simulation,  $N_{cv}$ , are reported in Table 1. A representation of the coarse mesh is shown in Figure 3(b). Figure 1(b) shows a Schlieren visualization of the shock formed over the Sandia ATB. There was no targeted refinement around the shock.

The boundary conditions of the simulation domain are as follows: The inlet is a plug flow at  $x/c = -34$ , where the inflow conditions are specified using the stagnation values of the temperature, pressure, and Mach number measurements at  $x/c \sim 0.65$  provided by Lynch *et al.* (2020), modified with the appropriate isentropic relations. This assumes that the flow between the inlet and the measurement point is isentropic, which is deemed a valid assumption since the measurement is upstream of the shock and is above the boundary layer. The outlet at  $x/c = 16$  is treated using a non-reflecting characteristic boundary condition with constant freestream pressure. The influence of the boundary conditions on the tunnel sidewalls was tested via a numerical experiment in which either an equilibrium turbulent stress or an inviscid wall boundary condition was used. It was found that the effect of this boundary condition on the shock location was weak. The results presented in this brief use the inviscid boundary condition on the wind tunnel walls and the equilibrium wall model with first-point matching on the Sandia ATB walls.

### 4. DSM results

The two engineering QoIs that are used to test the sensitivity of the WMLES solutions to SGS models are the skin-friction and pressure coefficients, defined as

$$C_f = \frac{\tau_w}{1/2\gamma p_0 Ma^2} \quad (4.1)$$

Mesh	$N_{cv}$	$\delta/\Delta$ (at $x/c = -0.78$ )
Coarse	60 million	9
Medium	200 million	12
Fine	780 million	16

TABLE 1. Mesh parameters for WMLES of the Sandia ATB at a chords Reynolds number of  $Re_c = 1 \times 10^6$  and  $Ma = 0.875$ .

and

$$C_p = \frac{p - p_0}{1/2\gamma p_0 Ma^2}, \quad (4.2)$$

where  $\gamma$ ,  $\tau_w$ ,  $p$ , and  $p_0$  are the heat capacity ratio, mean wall stress, wall pressure, and reference pressure, respectively. The reference pressure and Mach number are defined as the wall pressure and Mach number at  $x/c = 0$  as reported by Lynch *et al.* (2020). The results are compared to the new experimental measurements by Lynch (2022).

Figure 4 shows the  $C_f$  and  $C_p$  predictions for each of the three grid resolutions. The two coefficients exhibit different behaviors with grid refinement depending on the flow region. To understand their behaviors, we can partition the streamwise extent of the bump into four regions and examine the behavior independently in each. The first region extends over  $-0.5 \leq x/c < 0.2$  and covers a zero-to-adverse-to-favorable-pressure gradient attached turbulent boundary layer. The second region extends over  $0.2 \leq x/c < 0.6$  and covers the remainder of the favorable-pressure gradient, terminating with the shock/boundary layer interaction. The third region extends over  $0.6 \leq x/c < 1.25$ , which covers the separation bubble. Finally, the fourth region covers the reattachment region,  $1.25 \leq x/c \leq 2$ .

In the first region, both  $C_f$  and  $C_p$  exhibit near grid independence. Compared to the experiment, their predicted values in this region are within the experimental uncertainty bounds. For  $C_f$ , this indicates that the stress provided by the wall model is accurate even at coarse resolutions owing to an approximate satisfaction of its underlying equilibrium assumptions. However, there is a systematic over-prediction compared to the mean that persists with grid refinement. Section 5.1 shows that this is likely due to the upstream origin of the boundary layer, which in the experiment is tripped using a backward-facing step that is too small to resolve even at the finest grid resolutions.

In the second region,  $C_p$ , which is expected to be dominated by inviscid effects if thin boundary layer theory is invoked, follows the experimental measurements accurately. However,  $C_f$  does not agree with the measurements even at the finest resolution, and its peak exhibits non-monotonic behavior with grid refinement. This region can be further subdivided into  $0.2 \leq x/c < 0.4$  and  $0.4 \leq x/c < 0.6$ . In the first subregion, a continuation of the favorable-pressure gradient region, we observe monotonic convergence toward the experimental measurements. The remaining discrepancy between the solution at the finest grid and the experimental measurements is likely due to a combination of two effects. The first is the upstream origin of the boundary layer examined in section 5.1. The second is the zero-pressure gradient equilibrium assumption of the wall model. Within favorable-pressure gradient environments, the Reynolds shear stresses sustained by the turbulent boundary layer, and hence the skin friction, drop below those of an equivalent zero-pressure gradient boundary layer of the same thickness at the same Reynolds

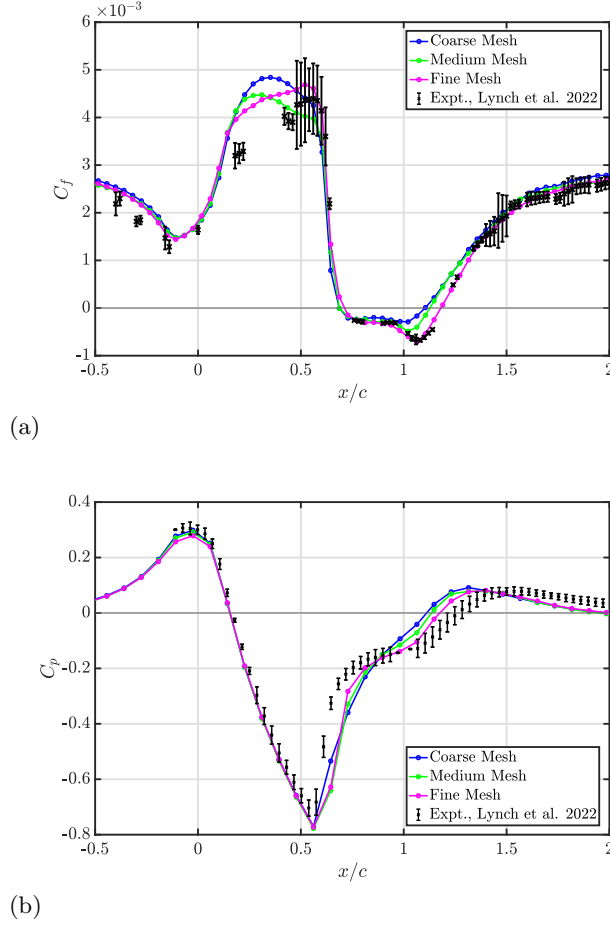


FIGURE 4. (a) The skin-friction coefficient,  $C_f$ , azimuthally averaged over the surface of the Sandia ATB as a function of the streamwise distance normalized by the chord length for each of the three mesh resolutions. (b) The pressure coefficient,  $C_p$ , extracted similarly. Both results use the equilibrium wall model with first-point matching and the DSM SGS model with local time averaging.

number. This effect can be qualitatively examined by considering the relaminarization parameter,  $K$ , which is a measure of the non-dimensional acceleration acting on the boundary layer, defined as

$$K = \frac{\mu}{\rho U_e^2} \frac{\partial U_e}{\partial s}, \quad (4.3)$$

where  $\mu$  is the dynamic viscosity,  $U_e$  is the boundary layer edge velocity, and  $s$  is the arc-length along the surface of the geometry. In zero-pressure gradient boundary layers,  $K$  is zero. Utilizing thin boundary layer approximations along with the compressible Bernoulli equation, we can show that  $K$  simplifies to

$$K = -\frac{1}{2Re_c} \frac{\partial C_p}{\partial s^*} \quad s^* = s/c, \quad (4.4)$$

which is plotted in Figure 5 using the experimental measurements on the Sandia ATB. Narasimha & Sreenivasan (1973) showed that for a value of  $K \geq 3 \times 10^{-6}$ , turbulent

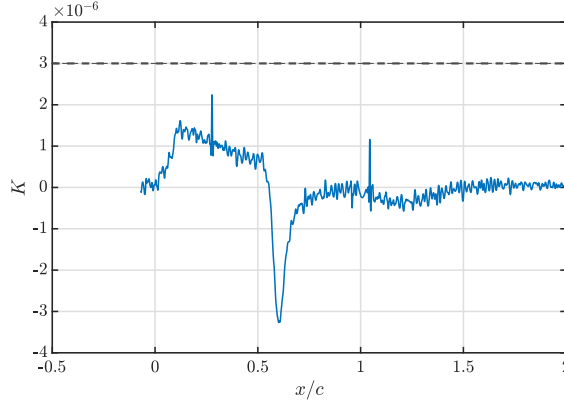


FIGURE 5. The relaminarization parameter,  $K = \frac{\mu}{\rho U_\infty^2} \frac{\partial U_\infty}{\partial s}$ , over the Sandia ATB computed using the experimental measurement of the pressure coefficient and the simplified definition in Eq. 4.4. The black horizontal dashed line indicates the empirical threshold for relaminarization of Narasimha & Sreenivasan (1973).

boundary layers fully relaminarize. While that is not the case for this flow,  $K$  is within a factor of two of this threshold, indicating a drop in Reynolds shear stresses. Hence, the stress predicted by the equilibrium wall model is likely overestimated.

In the second subregion, containing the skin friction peak and the shock/boundary-layer interaction, the WMLES calculations exhibit non-monotonic behavior with grid refinement, with the coarse grid skin friction passing through the mean of the experimental data, the medium grid under-predicting the stress, and the fine grid over-predicting the stress by the same amount, but with the correct streamwise evolution. It is hypothesized that this behavior is tied to the upstream behavior in both the first global region and the first subregion of the second region; in other words, it is not a local phenomenon and is likely to be partially fixed using a similar setup to the one presented in section 5.1. The correct prediction of the skin-friction coefficient in this subregion results from the accumulated effect of the pressure gradient distribution upstream on the resolved boundary layer (Bobke *et al.* 2017; Pozuelo *et al.* 2022). Since this boundary layer does not evolve correctly downstream on the coarse and medium grids, it is not affected correctly by the pressure gradient distribution, which is independent of the grid due to it being primarily an inviscid effect. Once this thin boundary layer is sufficiently resolved on the fine grid, the accumulated pressure-gradient effects become more physically accurate, and the streamwise behavior of the skin-friction coefficient adjusts to follow that of the experiment.

The third region of the flow contains the shock, the separation point, and the reattachment point of the separation bubble. Since the location of the shock is mostly an inviscid phenomenon that is accurately predicted as shown in Figure 4(b), and since the strength of this shock is sufficiently strong to cause almost instantaneous separation of the boundary layer, the location of the separation point is agnostic to the previous inaccuracies in the resolved boundary layer on the coarse and medium grids, and is therefore nearly grid-independent. The skin friction within the first half of the separation bubble,  $0.6 \leq x/c < 1$ , is the same regardless of the grid and follows the experimental measurement. On the other hand, the second half of the separation bubble,  $1 \leq x/c < 1.25$ , contains sharper gradients near the wall due to the direction of the circulation and its

streamwise inclination, requiring the fine resolution to predict the increased negative skin friction measured in the experiment. The fourth region of the flow, which constitutes the reattachment of the separated shear layer, is predicted quite accurately independently of the grid due to the weak pressure gradient acting on the attached boundary layer.

Overall, the WMLES prediction of the flow around the Sandia ATB using standard WMLES practices, i.e., using the equilibrium wall model and the DSM SGS model, is satisfactory and shows improvement compared to previous attempts in all regions of the flow once the boundary layer is resolved with  $\mathcal{O}(15\text{--}20)$  grid points.

## 5. DTCSM results

To test the sensitivity of the WMLES prediction to the choice/assumptions of the SGS model, specifically to the assumption of alignment between SGS stress and strain rate in typical eddy viscosity SGS models, the non-Boussinesq dynamic tensorial-coefficient eddy-viscosity SGS model of Agrawal *et al.* (2022) is used. The same geometry, grid resolutions, and boundary conditions are incorporated. Figure 6 shows the skin-friction coefficient,  $C_f$ , and pressure coefficient,  $C_p$ , along the streamwise extent of the bump. The flow is once again decomposed into the same four regions,  $-0.5 \leq x/c < 0.2$ ,  $0.2 \leq x/c < 0.6$ ,  $0.6 \leq x/c < 1.25$ , and  $1.25 \leq x/c < 2$ , and the effect of DTCSM SGS model is contrasted with the DSM SGS model of the previous section in each region.

In the first region,  $C_f$  is once again nearly independent of the grid resolution, indicating that the input to the wall model is within the logarithmic region of the flow at all grid resolutions, hence predicting the same wall-shear stress. However, the skin friction is substantially over-predicted compared to the simulations which use the DSM SGS model regardless of grid resolution. The turbulent boundary layer upstream of the bump transitions due to tripping over a backward-facing step at  $x/c = -2.52$ . The height of this backward-facing step is  $x/c = 0.002$  and is only partially resolved at the finest resolution. Therefore, there is an adjustment length over which the boundary layer contains numerical artifacts propagating downstream of the tripping location. We hypothesize that the DTCSM SGS model is more sensitive to these numerical artifacts, leading to a systematic misprediction of the skin-friction coefficient even in the nominally zero-pressure gradient region. Section 5.1 presents a test where a modified geometry is used to provide a sufficiently long adjustment length, where the DTCSM model outperforms the DSM model in this region. In the second region, the solutions are more independent of the grid resolution than those predicted using DSM. However, a systematic over-prediction is again hypothesized to be due to the numerical errors propagating from further upstream. The third and fourth regions, which encompass the separation bubble and the reattachment region, monotonically approach the experimental measurements with grid refinement. However, the separation point is no longer agnostic to the grid resolution.

The pressure coefficient is grid-independent in the first and second regions and monotonically approaches the experimental measurements in the third and fourth ones, similar to the DSM model results.

### 5.1. An experiment to remove the numerical errors originating upstream

To test whether the DTCSM SGS model is less accurate in this setting than the DSM SGS model due to an inherent deficiency or a heightened sensitivity to the incoming boundary layer, we modify the geometry and remove the wind tunnel, along with the backward-facing step, and adopt the near identical geometry of the experiment by Bachalo & Johnson (1986). We run the  $60^\circ$  sector geometry at the operating conditions of the



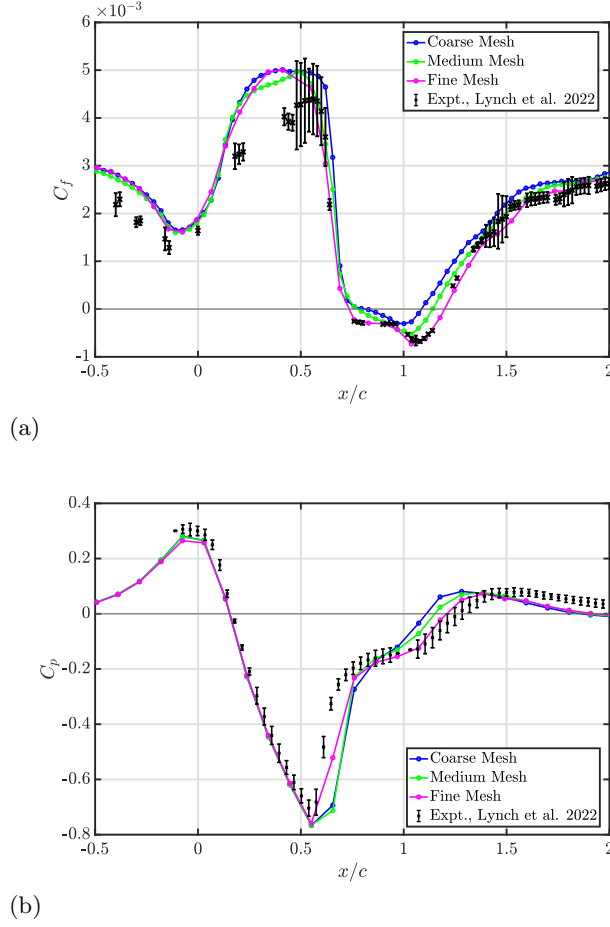


FIGURE 6. (a) The skin-friction coefficient,  $C_f$ , azimuthally averaged over the surface of the Sandia ATB as a function of the streamwise distance normalized by the chord length for each of the three mesh resolutions. (b) The pressure coefficient,  $C_p$ , extracted similarly. Both results use the equilibrium wall model with first-point matching and the DTCSM SGS model with local time averaging.

Sandia ATB, namely  $Re_c = 1 \times 10^6$  and  $Ma = 0.875$ , and extend the upstream cylindrical region sufficiently far for the numerical artifacts to disappear. In this case, the inflow is prescribed as a plug flow at  $x/c = -8$ .

Figure 7 shows the skin-friction coefficient using the equilibrium wall model and the DTCSM SGS model at the same grid resolution per boundary layer thickness as the full wind tunnel calculations. The skin-friction coefficient now converges monotonically, passes through the experimental measurements upstream of the bump, and maintains the continued upward trajectory in the range  $0 \leq x/c < 0.6$  for all grid resolutions, which was previously observed only at the fine grid with DSM. This strengthens the hypothesis that DTCSM outperforms the DSM SGS model within a healthy turbulent flow but is more sensitive to numerical artifacts. Note that the shock and the separation bubble,  $0.6 \leq x/c < 1.25$ , are weaker than those found in the Sandia ATB case, which includes the wind tunnel. This is due to the larger blocking effect in the Sandia ATB experiment compared to the NASA ATB experiment by Bachalo & Johnson (1986).

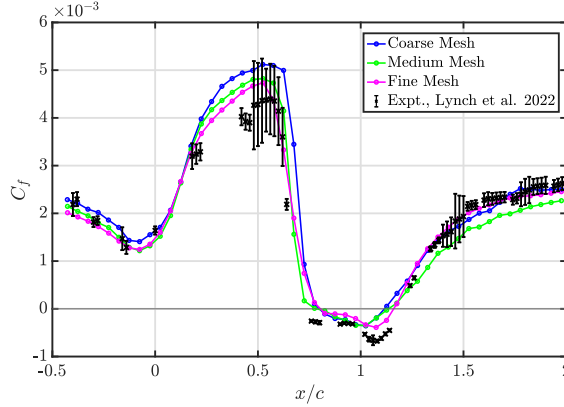


FIGURE 7. The skin-friction coefficient,  $C_f$ , azimuthally averaged over the surface of the upstream extended  $60^\circ$  sector Bachalo-Johnson geometry with the Sandia ATB operating conditions,  $Re_c = 1 \times 10^6$  and  $Ma = 0.875$ , as a function of the streamwise distance normalized by the chord length for each of the three mesh resolutions.

## 6. Conclusions and future work

The Sandia ATB experiment, similar to the Bachalo & Johnson (1986) NASA ATB, provides a canonical case at transonic flow conditions representative of flows over commercial aircraft to test the predictive capabilities of various CFD paradigms. In particular, its moderate Reynolds number is accessible to high-fidelity simulations. In this work, we used WMLES to simulate the Sandia ATB experiment and tested the solutions' sensitivity to the SGS model choice. The experimental setup was simulated faithfully, including the effects of the wind tunnel. The two dynamic SGS models used were the single-coefficient DSM and the non-Boussinesq tensorial-coefficient DTCSM model. Their performance was quantified by scrutinizing the predictions of two key engineering QoIs: the skin-friction coefficient,  $C_f$ , and the pressure coefficient,  $C_p$ . The equilibrium wall model with first grid-cell matching was used for all cases.

The simulations utilizing the DSM SGS model exhibited different grid convergence behaviors depending on the region of the flow. The zero-to-adverse-to-favorable-pressure gradient region, the shock and separation point locations, and the reattachment behavior were all captured accurately and were grid-independent. However, the skin-friction coefficient behaved non-monotonically with grid refinement at the apex of the bump where the skin friction peak is.

The DTCSM SGS model can carry anisotropic stress which modifies the flow dynamically, and is therefore expected to be more grid-independent at coarser resolutions. Indeed, skin-friction and pressure coefficient predictions were found to be more grid-independent up to the location of the shock. However, there is a systematic overshoot that does not go away with grid refinement. This was traced to the numerical artifacts originating from the mechanism used to trip the boundary layer upstream. Since the backward-facing step was too small to resolve accurately, a secondary test where it was removed and the boundary layer was allowed to develop over a longer distance was conducted. It showed that the DTCSM model is more accurate and can predict monotonically converging results with the correct behavior.

Overall, it was found that WMLES with dynamic SGS models can accurately predict the flow over the Sandia ATB with reasonable accuracy given  $\mathcal{O}(15)$  grid points per

upstream boundary layer. The DTCSM SGS model, which allows for non-Boussinesq effects to be captured, was found to be more accurate but also more sensitive to the structure of the resolved turbulent flow used as an input to the model than the DSM SGS model.

## Acknowledgments

This investigation was funded by NASA grant #80NSSC20M0201. Computational resources were provided by the Oak Ridge Leadership Computing Facility. The authors thank Dr. K. Lynch of Sandia National Laboratory for providing the new experimental measurements.

## REFERENCES

- AGRAWAL, R., WHITMORE, M. P., GRIFFIN, K. P., BOSE, S. T. & MOIN, P. 2022 Non-Boussinesq subgrid-scale model with dynamic tensorial coefficients. *Phys. Rev. Fluids* **7**, 074602.
- BACHALO, W. & JOHNSON, D. 1986 Transonic, turbulent boundary-layer separation generated on an axisymmetric flow model. *AIAA J.* **24**, 437–443.
- BERESH, S. J., BARONE, M. F., DOWDING, K., LYNCH, K. P. & MILLER, N. E. 2020 A CFD validation challenge for transonic, shock-induced separated flow: approach and metrics. *AIAA Paper* 2020-1308.
- BOBKE, A., VINUESA, R., ÖRLÜ, R. & SCHLATTER, P. 2017 History effects and near equilibrium in adverse-pressure-gradient turbulent boundary layers. *J. Fluid Mech.* **820**, 667–692.
- BOSE, S. T. & PARK, G. I. 2018 Wall-modeled large-eddy simulation for complex turbulent flows. *Annu. Rev. Fluid Mech.* **50**, 535–561.
- CHOI, H. & MOIN, P. 2012 Grid-point requirements for large eddy simulation: Chapman’s estimates revisited. *Phys. Fluids* **24**, 011702.
- GERMANO, M., PIOMELLI, U., MOIN, P. & CABOT, W. H. 1991 A dynamic subgrid-scale eddy viscosity model. *Phys. Fluids A* **3**, 1760–1765.
- GOC, K. A. 2023 *Towards Certification by Analysis: Large Eddy Simulations of Commercial Aircraft across the Flight Envelope.*, PhD Thesis.
- GOC, K. A., LEHMKUHL, O., PARK, G. I., BOSE, S. T. & MOIN, P. 2021 Large eddy simulation of aircraft at affordable cost: a milestone in computational fluid dynamics. *Flow* **1**, E14.
- GUPTA, M., DATTA, A., MATHEW, J. & HEMCHANDRA, S. 2021 Shock induced separation in a transonic flow past an axi-symmetric hump. *AIAA Paper* 2021-2756.
- KAWAI, S. & LARSSON, J. 2013 Dynamic non-equilibrium wall-modeling for large eddy simulation at high Reynolds numbers. *Phys. Fluids* **25**, 015105.
- LEE, H. C. & PULLIAM, T. H. 2019 Overflow juncture flow computations compared with experimental data. *AIAA Paper* 2019-0080.
- LILLY, D. K. 1992 A proposed modification of the Germano subgrid-scale closure method. *Phys. Fluids A* **4**, 633–635.
- LOZANO-DURÁN, A., BOSE, S. T. & MOIN, P. 2020 Prediction of trailing edge separation on the NASA Juncture Flow using wall-modeled LES. *AIAA Paper* 2020-1776.
- LOZANO-DURÁN, A., BOSE, S. T. & MOIN, P. 2022 Performance of wall-modeled LES

- with boundary-layer-conforming grids for external aerodynamics. *AIAA J.* **60**, 747–766.
- LYNCH, K. 2022 Experimental characterization of an axisymmetric transonic separated flow for CFD validation. *AIAA J.* under review.
- LYNCH, K. P., BARONE, M. F., BERESH, S. J., SPILLERS, R., HENFLING, J. & SOEHNEL, M. 2019 Revisiting Bachalo-Johnson: the sandia axisymmetric transonic hump and CFD challenge. *AIAA Paper* 2019-2848.
- LYNCH, K. P., LANCE, B., LEE, G. S., NAUGHTON, J. W., MILLER, N. E., BARONE, M. F., BERESH, S. J., SPILLERS, R. & SOEHNEL, M. 2020 A CFD validation challenge for transonic, shock-induced separated flow: experimental characterization. *AIAA Paper* 2020-1309.
- MENEVEAU, C. & KATZ, J. 2000 Scale-invariance and turbulence models for large-eddy simulation. *Annu. Rev. Fluid Mech.* **32**, 1–32.
- NARASIMHA, R. & SREENIVASAN, K. 1973 Relaminarization in highly accelerated turbulent boundary layers. *J. Fluid Mech.* **61**, 417–447.
- POZUELO, R., LI, Q., SCHLATTER, P. & VINUESA, R. 2022 An adverse-pressure-gradient turbulent boundary layer with nearly constant  $\beta \simeq 1.4$  up to  $Re_\theta \simeq 8700$ . *J. Fluid Mech.* **939**, A34.
- RAHMANI, S. K. & WANG, Z. J. 2022 Large eddy simulation of the sandia axisymmetric transonic hump using a high-order method. *AIAA Paper* 2022-1534.
- RILEY, L. P. & ADLER, M. 2021 RANS and wall-modeled LES predictions for the Sandia challenge on transonic, separated flow. *AIAA Paper* 2021-2757.
- ROGALLO, R. S. & MOIN, P. 1984 Numerical simulation of turbulent flows. *Annu. Rev. Fluid Mech.* **16**, 99–137.
- RUMSEY, C. L., SLOTNICK, J. P. & SCLAFANI, A. J. 2019 Overview and summary of the Third AIAA High Lift Prediction Workshop. *J. Aircraft* **56**, 621–644.
- TOWNSEND, A. 1976 *The Structure of Turbulent Shear Flow*. Cambridge University Press.
- VASSBERG, J., DEHAAN, M., RIVERS, M. & WAHLS, R. 2008 Development of a common research model for applied CFD validation studies. *AIAA Paper* 2008-6919.
- YANG, X. I. A. & GRIFFIN, K. P. 2021 Grid-point and time-step requirements for direct numerical simulation and large-eddy simulation. *Phys. Fluids* **33**, 015108.